ACS APPLIED MATERIALS & INTERFACES

Research Article

www.acsami.org

Surface Modification of TiO_2 Nanocrystals by WO_x Coating or Wrapping: Solvothermal Synthesis and Enhanced Surface Chemistry

Mauro Epifani,*[,†] Raül Díaz,[‡] Carmen Force,[§] Elisabetta Comini,[∥] Marta Manzanares,[⊥] Teresa Andreu,[⊥] Aziz Genç,[#,♦] Jordi Arbiol,[#,⊗,♦] Pietro Siciliano,[†] Guido Faglia,[∥] and Joan R. Morante[⊥,○]

[†]Istituto per la Microelettronica e i Microsistemi, IMM-CNR, Via Monteroni, 73100 Lecce, Italy

[‡]Electrochemical Processes Unit, IMDEA Energy Institute, Avda. Ramón de la Sagra 3, 28935 Móstoles, Spain

[§]NMR Unit,Centro de Apoyo Tecnológico, Universidad Rey Juan Carlos, c/Tulipán, s/n, 28933 Móstoles, Spain

[∥]SENSOR Lab, Department of Information Engineering, Brescia University and CNR-INO, Via Valotti 9, 25133 Brescia, Italy

[⊥]Catalonia Institute for Energy Research, IREC, Universitat de Barcelona, c/Jardins de les Dones de Negre 1, 08930 Sant Adria del Besos, Barcelona, Spain

[#]Institut de Ciència de Materials de Barcelona, ICMAB-CSIC, Campus de la UAB, 08193 Bellaterra, Spain

[⊗]Institució Catalana de Recerca i Estudis Avançats (ICREA), Passeig Lluís Companys 23, 08010 Barcelona, CAT Spain

[○]M2E-IN2UB-XaRMAE, Departament d'Electrònica, Universitat de Barcelona, c/Martí i Franquès 1, 08028 Barcelona, Spain

[♦]Institut Català de Nanociència i Nanotecnologia (ICN2), Campus UAB, 08193 Bellaterra, Catalonia, Spain

Supporting Information

ABSTRACT: TiO_2 anatase nanocrystals were prepared by solvothermal processing of Ti chloroalkoxide in oleic acid, in the presence of W chloroalkoxide, with W/Ti nominal atomic concentration (R_w) ranging from 0.16 to 0.64. The as-prepared materials were heat-treated up to 500 °C for thermal stabilization and sensing device processing. For $R_{0.16}$, the as-prepared materials were constituted by an anatase core surface-modified by WO_x monolayers. This structure persisted up to 500 °C, without any WO_3 phase segregation. For R_w up to $R_{0.64}$, the anatase core was initially wrapped by an amorphous WO_x gel. Upon heat treatment, the WO_x phase underwent structural reorganization, remaining amorphous up to 400 °C and forming tiny WO_3 nanocrystals dispersed into the TiO_2 host after heating at 500 °C, when part of tungsten also migrated into the TiO_2 structure, resulting in structural and electrical modification of the anatase host. The ethanol sensing properties of the various materials were tested and compared with pure TiO_2 and WO_3 analogously prepared. They showed that even the simple surface modification of the TiO_2 host resulted in a 3 orders of magnitude response improvement with respect to pure TiO_2.

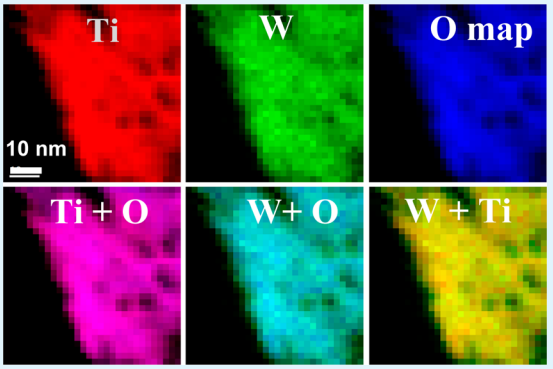

KEYWORDS: *TiO_2, solvothermal synthesis, metal oxide nanocrystals, surface modification, gas sensors, nanocomposites*

INTRODUCTION

TiO_2–WO_3 composite materials have, for a long time, been known as efficient catalysts for selective catalytic reduction of NO_x,[1−4] but they have also been used for other reactions such as isomerizations,[5−7] isopropanol dehydration,[8] and glycerol conversion,[9−11] just to mention a few additional examples. Even the photocatalytic properties were well-known,[12−16] and they have been recently attracting increasing attention.[17−22] Further applications concern the gas-sensing properties.[23,24] All these applications rely on a synergistic interaction between the WO_x species and the surface of the TiO_2 support. It is then not surprising that intensive efforts have been devoted in the past to the investigation of the structure of such species as a function of the tungsten concentration, dehydration conditions, heat-treatment temperature, and of all the parameters that may determine their distribution and evolution. In the large majority of these studies, the TiO_2 support was constituted by commercial P25 samples, or other kind of material typologies,[25] where the grain size of the TiO_2 was beyond the nanosized regime,[25,26] and typical synthesis approaches included coprecipitation and impregnation. Other synthesis procedures were also investigated. Engweiler et al. used grafting of W alkoxides but onto commercial P25 titania.[1] Puddu et al. used hydrothermal synthesis to directly prepare TiO_2–WO_3 nanocomposites.[14] Sol–gel coprocessing of titanium alkoxides and other tungsten precursors was also applied.[3,15,20,27] The

Received: January 21, 2015
Accepted: March 16, 2015
Published: March 16, 2015

DOI: 10.1021/acsami.5b00632
ACS Appl. Mater. Interfaces 2015, 7, 6898−6908

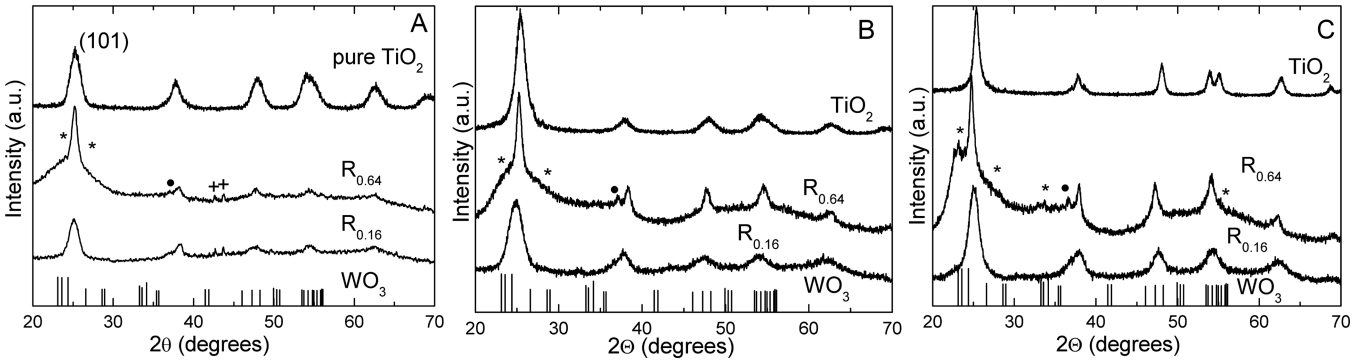

Figure 1. XRD patterns of the as-prepared (A), 400 °C (B), and 500 °C (C) samples. For WO_3, the positions of the most intense reflections of the monoclinic phase (JCPDS 00−043−1035) are indicated. The symbols indicate the reflections not attributable to anatase (see text).

material architecture could anyway be described by titania base material whose surface was covered by WO_x species, possibly not affecting the whole surface for low W concentrations. In these cases, the size of the anatase grains dominates the materials architecture: simply, when the surface capacity of accommodating tungsten oxide monolayers is exhausted, the WO_3 particles begin to segregate. It seems that TiO_2 colloidal nanocrystals, whose size should be comparable with that of any WO_3 segregated species, have never been considered as host material. This topic is of remarkable interest for different reasons. From a fundamental point of view, we wondered what happens if the TiO_2 support is constituted by colloidal nanocrystals, whose size becomes comparable to the segregated WO_3 phase. This question was suggested by previous work on the TiO_2−V_2O_5 system, showing the possibility of coating the surface of anatase nanocrystals with vanadium oxide species.[28] The chemistry of the vanadium precursor prevented the precipitation of vanadium oxide grains up to at least 400 °C. The analogous W precursor has a markedly different chemistry, enhancing the formation of W oxides.[29] Hence, the aim was to explore which kind of structures could be obtained in this case. We will show that, with respect to the existing works, the developed synthesis not only preserves the nanosized TiO_2 base material, but results in different architectures, ranging from surface modification to wrapping by WO_x gel. This result has remarkable interest even from an applicative point of view. We originally developed the synthesis for gas-sensing field, where it is now well-established that nanosized oxide grains may remarkably boost the performance of chemoresistive gas-sensors. Nevertheless, if the TiO_2 core has remarkably larger size than the WO_x guest material, the electrical and sensing performance will still be dominated by those of TiO_2, since the WO_x phase will only constitute an extremely thin part of the overall material structure. The use of colloidal nanocrystalline TiO_2 paves the way to an enhanced synergistic effect, since now the WO_x contribution becomes more comparable to the TiO_2 base material. Indeed, we obtained a fully nanosized version of the TiO_2−WO_x catalyst: even after heating at 500 °C, the mean grain size was 8−10 nm. We will show that electrical and sensing properties of the resulting materials were remarkably modified by the presence of the WO_x species, with gas-response enhancement ranging over orders of magnitude. The success of the sensing application was meant only to further establish and develop the approach of inorganic surface modification by another oxide, which is novel in gas-sensing field and enables further interesting applications. From a more general point of view, we will show the effectiveness of coupling an architecture that is of interest for heterogeneous catalysis itself with a field like gas sensors where the surface reactions are of primary importance. Moreover, the set of the obtained results was the starting point for clarifying the difference between oxide heterojunctions and surface monolayers.

EXPERIMENTAL SECTION

The synthesis strategy comprised two steps: first amorphous TiO_2 nanoparticles were synthesized by sol−gel process,[30] and then they were crystallized in a solvothermal step where the tungsten precursor was also added. The first step was described in detail in previous work.[28] The following solvothermal crystallization step[28] was performed for 2 h at 250 °C after dispersing the TiO_2 nanoparticles in 10 mL of oleic acid. In this step, a given volume, ranging from 0.5 to 2 mL, of tungsten chloromethoxide solution was added before the solvothermal heating, for preparing TiO_2−WO_3 materials. The tungsten precursor was prepared as described in previous work,[29] starting from WCl_6 and methanol. The W-modified samples will be denoted with the R_x code, where x, indicating the nominal W/Ti atomic concentration, ranged from 0.16 to 0.64. After the solvothermal step, the synthesis product was extracted with methanol and purified with acetone.

X-ray diffraction (XRD) patterns, Fourier transform infrared (FTIR) and Raman measurements, and thermal analyses were obtained with the previously described setup.[28]

Solid-state NMR spectra of $^{47/49}$Ti (22.53 MHz) were obtained using a Varian Infinity 400 spectrometer operating at 400 MHz with 9.395 T, using a probe with a 7 mm coil in static conditions. The sequence used to obtain the spectra was two pulses Hahn spin−echo with phase cycle. The pulse was 40 μs in duration. The delay between scans was 1, and 20.000 scans were collected for each spectrum. The titanium NMR spectra were referenced against the standard titanium isopropoxide. This compound is shifted (−850 ppm) against the conventional shift standard for titanium $TiCl_4$ (0 ppm).

X-ray photoelectron spectroscopy (XPS) was performed using a PHI ESCA-5500 equipment working with the Al Kα radiation (1486.6 eV).[28] The powders were fixed on the sample holder with a biadhesive tape, giving them a certain amount of surface charging on all of the peak positions of the main narrow scan spectra acquired: W 4f, Ti 2p and Ti 3p, O 1s, C 1s. They were all properly corrected with respect to the adventitious C 1s present on the surface with respect to the tabulated and literature value of 284.6 eV.

High-resolution transmission electron microscopy (HRTEM) analyses of the powders were obtained with a previously described setup,[28] consisting in a field emission gun microscope FEI Tecnai F20, working at 200 kV and with a point-to-point resolution of 0.19 nm. Scanning transmission electron microscopy (STEM) in high angle annular dark field (HAADF) mode combined with electron energy loss spectroscopy (EELS) spectrum imaging were also obtained in the same FEI Tecnai F20.

DOI: 10.1021/acsami.5b00632
ACS Appl. Mater. Interfaces 2015, 7, 6898−6908

The gas-sensing tests were performed on the materials heat-treated at 500 °C by using the previously described standard configuration for resistive sensor measurement and the same fabrication procedure.[28] The sensor devices were placed in a sealed chamber with a constant flux of 0.3 L/min of humid synthetic air (40% relative humidity (RH) at 20 °C) into which the desired amount of test gases was mixed. The sensor response was defined as $(G_{gas} - G_0)/G_0$, where G_0 was the sensor baseline electrical conductance in synthetic air, and G_{gas} indicated the sensor electrical conductance after exposure to the target gas. Ethanol was tested in concentrations ranging from 50 to 500 ppm. Ethanol is a classical choice as a gas of relevant practical interest, but above all we wanted a gas to be compared with our previous TiO_2–V_2O_5 work,[28] where ethanol had been chosen in agreement with the organics oxidation activity of TiO_2–V_2O_5 classical catalyst. In this way, the principle of catalytic surface activation by deposition of another oxide could be tested and possibly reinforced. The sensing devices selected for the gas tests had base conductance values dispersed within 10% of the results showed in the manuscript. In this case, the measured responses were also comprised in such range. Error bars were hence not included in the plots for the sake of clarity. Repeated experiments under the same operational conditions yielded stable and reproducible sensor responses for several months (estimated uncertainty = ±10%). For comparison, the response of previously investigated devices based on pure TiO_2[28] and WO_3[31] was also considered.

RESULTS AND DISCUSSION

1. Structure and Structural Evolution of the Materials as a Function of R_w. The XRD patterns of the as-prepared samples with various R_w values are reported in Figure 1. Other R_w values were investigated, but there were no obvious differences between the related XRD patterns (Figure S1, Supporting Information), so only $R_{0.16}$ and $R_{0.64}$ were considered throughout the rest of the work. The pattern of the $R_{0.16}$ sample was very similar to that of pure TiO_2, apart for a few weak additional peaks. The remaining peak positions were in agreement with those of pure TiO_2 in the anatase crystallographic phase.

The $R_{0.64}$ sample showed, at low angles, additional signals overlapped with the (101) anatase peak. Other additional peaks, in the same positions of those observed in the $R_{0.16}$ pattern, are also indicated. The broad, low-angle peaks marked with a star were in agreement with the JCPDS data for various WO_x compounds. Nevertheless, only the most intense reflections of WO_3 and tungsten titanate ($Ti_{0.54}W_{0.46}O_2$, JCPDS: 98–004–4652) occurred where marked by stars and a full circle, respectively, in the figure. Other peaks of the titanates could be overlapped with anatase; anyway, not all of the expected peaks were observed. After the material was heated at 400 °C, no different reflections were observed. Only the peaks indicated with crosses, related to an unidentified phase in the as-prepared samples, disappeared. After the material was heated at 500 °C, the main (101) anatase peak was shifted to lower angles for $R_{0.64}$, while the WO_3 peaks at lower angles were more resolved, and new ones appeared, indicated in the figure with further stars. For $R_{0.16}$ only the anatase pattern was still observed, apart for the additional peak at $2\theta \approx 37°$, present at all the considered temperatures. For $R_{0.64}$, the situation was more complex. After the material was heated at 500 °C the (105) and (211) peaks at ca. 53–55° did not split (Figure 1C), and the (101) peak at ~25° was visibly shifted to lower angles. We note that the tungsten titanate phase, indicated with a solid circle, was always present, even after heating at high temperatures, above all for $R_{0.64}$, without remarkable relative intensity variations.

We believe that this phase was a byproduct of the reaction of the W precursor with the Ti oxide species generated in the solvothermal step by the dissolution–re-precipitation processes of the TiO_2 nanoparticles, since (i) formation of such phase occurred already in the as-prepared materials, where diffusion of the W^{6+} cations into the anatase structure would be unlikely; moreover, (ii) should diffusion occur, it would not be understood why only a small fraction of the titanate phase was actually present. The Raman spectra of the same samples were measured, expecting them to be more sensitive to modifications of the crystal structure. The spectra are shown in Figure 2. In the as-prepared samples, apart for the anatase

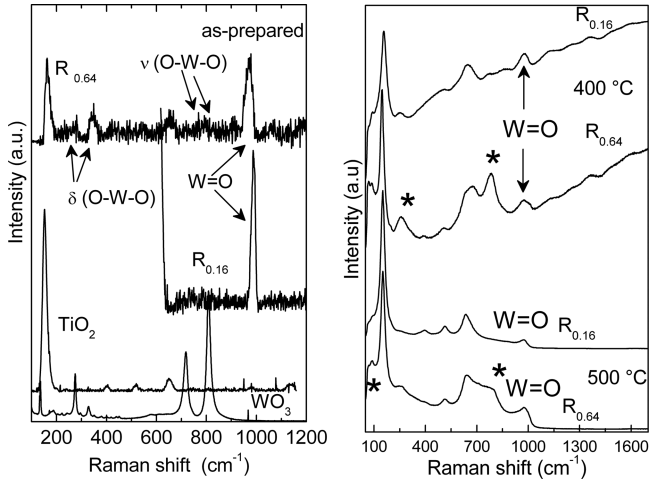

Figure 2. Raman spectra measured on the as-prepared (left), 400 °C, and 500 °C (right) samples. The Raman spectra of pure TiO_2 and WO_3 are reported as a reference in the as-prepared spectra.

Raman features, bands at ~274 and 330 cm^{-1} were present for both W concentrations, and more clearly for $R_{0.64}$. They were attributed[32] to the δ (O–W–O) modes, while weak bands overlapped to the background in the 800 cm^{-1} region suggest the ν (O–W–O) modes. Finally, a strong band was observed at 1007 and 974 cm^{-1} for $R_{0.16}$ and $R_{0.64}$, respectively. For $R_{0.16}$, the 1007 cm^{-1} band could be observed only when the rest of the anatase signal saturated; hence, the complete spectrum is shown in the Supporting Information (Figure S2).

The band is due to the W═O stretching mode of surface-dispersed tungsten oxide species.[1,33−40] The position and evolution of this band can give useful hint about the surface WO_x surface coverage, as we will see in the following. Hence, we will focus our attention to its position, which is summarized in Table 1 for all the samples. For completeness, we will only further remark on the non-anatase bands in heat-treated samples, which were marked by a star in Figure 2 (right). First of all, bands appeared at low frequency in similar positions to lattice modes of WO_3 (below ~100 cm^{-1}). A broad and strong band was found in the δ (O–W–O) region at ~250 cm^{-1} and, for $R_{0.64}$, at 785 cm^{-1}, in the ν(O–W–O) region. Moreover, after heating at 500 °C, there was no more organic residuals signal (see discussion below for 400 °C). Figure 3 shows representative TEM observations of as-prepared and 500 °C samples. The structure found in the as-prepared $R_{0.16}$ sample was TiO_2 tetragonal anatase. In the analogous $R_{0.64}$ sample, surprisingly, HRTEM showed that the material was composed of small amorphous clusters. HRTEM did not show crystal planes in any of the small nanostructures (nanoparticle-like).

DOI: 10.1021/acsami.5b00632
ACS Appl. Mater. Interfaces 2015, 7, 6898–6908

Table 1. W═O Raman Position for the Indicated Samples

sample	W═O position (cm^{-1})	attribution
as-prepared $R_{0.16}$	1007	tetrahedral W species
as-prepared $R_{0.64}$	974	tetrahedral and octahedral W species
400 °C $R_{0.16}$	977	tetrahedral and octahedral W species, increased fraction of octahedral sites
400 °C $R_{0.64}$	974	tetrahedral and octahedral W species, increased fraction of octahedral sites
500 °C $R_{0.16}$	974	tetrahedral and octahedral W species
500 °C $R_{0.64}$	974	tetrahedral and octahedral W species

Only in rare cases we could find some crystallized regions showing anatase-like plane distances.

The 500 °C $R_{0.16}$ sample comprised micron/submicron sized agglomerates (due to the thermal elimination of the organic capping) of ca. 7−10 nm spheroidal nanoparticles. Figure 3C shows a general HRTEM micrograph where different single crystalline nanoparticles in the agglomerate are present. Upper right is a close-up of a 10 nm single crystalline nanoparticle, and lower right is its corresponding power spectrum (FFT), which reveals that this nanoparticle has a TiO_2 anatase phase (space group = $I4_1/amd$) with lattice parameters of $a = b = 0.3785$ nm and $c = 0.9514$ nm and viewed along [1−11] direction. Obviously, even the 500 °C $R_{0.64}$ sample comprised micron/submicron sized agglomerates, with ∼10 nm spheroidal nanoparticles, as shown in the Supporting Information. The most surprising result was that the segregated WO_3 nanocrystals could not be distinguished into the TiO_2 host. On the other hand, the obtained *d*-spacing values could also fit for a monoclinic WO_3 phase, but the error margin was much larger for the case of WO_3 phase (fitting error is 8%). So, TiO_2 phase with a fitting error of ∼3% was more likely. This 3% error was due to measured *d*-spacing values that were larger than those of TiO_2 anatase phase, which might suggest the formation of doped TiO_2, solid solutions, or even new phases.

The formation of different oxides had already been suggested by the XRD patterns, so XPS was employed for analyzing more in detail the oxidation states of W in the as-prepared samples. Tungsten has different possible oxidation states, W^{6+} being the most common, but easily presenting substoichiometric oxides such has $W_{18}O_{49}$ or $W_{25}O_{73}$. W 4f has a spin−orbit doublet ($4f_{7/2}$ and $4f_{5/2}$) with intensity ratio 4:3 (fixed parameter), change in binding energy (ΔBE) of 2.1 eV (fixed parameter), and full width at half-maximum (fwhm) value of 1.6 eV (fixed parameter) except for the substoichiometric $4f_{7/2}$ contribution, which has an expected value of ∼1.8 eV. Then, four contributions from the W 4f were used, with expected BE values at 35.5 and 37.6 eV (for WO_3) and 34.3 and 36.5 eV (for WO_x species).[41,42] Titanium presents also a photopeak in the same energy range (Ti 3p has a BE ≈ 37.0 eV) and was also included as a contribution in the fitting process.[43,44] Additionally to W 4f contribution, a component corresponding to the W 5p3/2 peak must be factored. The W 5p3/2 peak was set at 5.5 eV above the W 4f7/2 peak. Finally, the shape of the spectra suggested the presence of a tungsten−titanium mixed phase ($W_xTi_yO_z$) with two photopeaks at ∼39.0 and 42.0 eV. Summarizing, W 4f spectra were fitted through eight contributions, and the results are reported in Table 2. The figures and the related fits are reported in the Supporting Information, together with the full results for Ti 2p. The ratio W^{6+}/W^{n+} for each individual peak 4f7/2 and 4f5/2 is 7.3 for $R_{0.16}$ and 4.2 for $R_{0.64}$, indicating than the amount of W^{n+} is higher in the $R_{0.64}$ sample. The relative intensity of Ti 3p peak is lower for $R_{0.64}$, which is consistent with the higher content of W in the sample. The relative amount of tungsten−titanium mixed

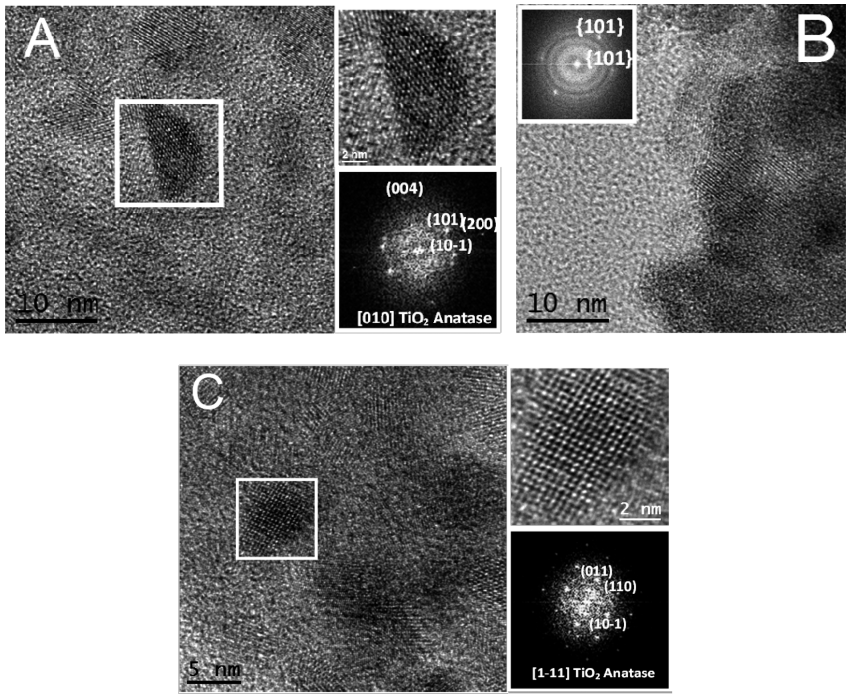

Figure 3. HRTEM images of as-prepared (A) $R_{0.16}$, (B) $R_{0.64}$, and 500 °C (C) $R_{0.16}$ samples. The insets show magnifications of the white-squared regions, with the related power spectra.

DOI: 10.1021/acsami.5b00632
ACS Appl. Mater. Interfaces 2015, 7, 6898−6908

Table 2. Results of the XPS Fitting on the Indicated Samples

	as-prepared $R_{0.16}$			as-prepared $R_{0.64}$		
band	BE (eV)	fwhm	%area	BE (eV)	fwhm	%area
W^{n+} (4f7/2)	34.25	1.85	5.28	34.25	1.9	9.33
W^{6+} (4f7/2)	35.55	1.65	38.68	35.46	1.67	39.06
W^{n+} (4f5/2)	36.35	1.65	3.96	36.35	1.67	7
Ti 3p	36.95	1.6	8.61	36.95	1.65	5.35
W^{6+} (4f5/2)	37.65	1.65	29.01	37.56	1.67	29.29
Ti−O−W	38.95	2.1	10.43	38.95	2.05	6.78
W 5p3/2	41.05	2.08	2.47	41.05	1.95	2.34
Ti−O−W	42.05	2.3	1.56	42.05	2.25	0.86

phase is higher for the $R_{0.16}$ sample. After the XPS results, we will describe the tungsten oxide phases found in the present work with the generic formula WO_x.

On the basis of the experimental data described, we could describe the materials evolution as follows. The as-prepared samples were constituted (XRD) by anatase nanocrystals mixed, for $R_{0.64}$, with amorphous and/or very small tungsten oxide species, whose structure resembled that of monoclinic WO_3. Figure 3B clarifies that, for $R_{0.64}$, the anatase nanocrystals, whose presence could only be ensured by the results of Figures 1 and 2, were "wrapped" by amorphous WO_x species, which occurred due to the high W concentration. In fact, the XPS data in Table 2 for $R_{0.64}$, for which the Ti/W signal ratio was less than one, clearly indicate that the TiO_2 nanocrystals are buried into the WO_x gel. We use the WO_x description in agreement with the indications of the XPS data, where it appeared that the $R_{0.64}$ sample contained a higher concentration of substoichiometric W species (with respect to WO_3). For R_w = 0.64, the outer regions of the WO_x aggregates are less influenced by the presence of the TiO_2 core, and their composition resembles that of chloroalkoxide-derived tungsten oxides, where the presence of substoichiometric species is typical.[29] The TiO_2 wrapping is an interesting phenomenon and was made possible by the remarkable hydrolytic instability of the W chloroalkoxide, whose molecules may self-cross-link instead of bonding to the anatase surface. On the other hand, in the same experimental solvothermal conditions, we could synthesize pure WO_3 quantum dots in the monoclinic phase, with a mean size of 4 nm.[31] From these observations, we concluded that phase separation of W oxide species occurred in the solvothermal step due to self-polymerization of the W precursor, but the TiO_2 nanoparticles interfered with the formation of the WO_3 structure, resulting in smaller species (very broad XRD reflections) whose composition was not the conventional WO_3 oxide. The Raman data allowed clarifying more in detail the structure of the as-prepared samples. The most prominent features of Figure 2A were the surface W═O stretching bands at 1007 cm^{-1} for $R_{0.16}$ and at 974 cm^{-1} for $R_{0.64}$. The position depends on the W local coordination.[34] As summarized in Table 1, peaks above 980 cm^{-1} in the hydrated environment of the present work were attributed to tetrahedral WO_4 species.[34] Hence, for $R_{0.16}$ the surface was covered with W═O species with distorted tetrahedral geometry. The band position for $R_{0.64}$, instead, suggested a more complex environment, including distorted octahedral sites, as previously discussed for high-coverage case,[34] to which the $R_{0.64}$ case could be assimilated. Octahedral sites are in agreement with the gel-like WO_x layer, with higher extent of cross-linking. In fact, the (O−W−O) modes in the Raman spectra corroborated the view of a dense layer of WO_x. In particular, it seemed reasonable to attribute the stronger signal of the bending modes with respect to the stretching ones to the two-dimensional structure of the WO_x layer. In the XPS data, the more intense Ti−O−W signal in $R_{0.16}$ with respect to $R_{0.64}$ was attributed to the signal attenuation due to the anatase wrapping by WO_x. In this frame, further magic-angle spinning NMR data (Supporting Information) supported a view where the anatase nanocrystals had an increasingly affected surface with increasing W concentration, in such a way that for $R_{0.16}$ the Ti signal was slightly more defined, while for $R_{0.64}$ their local coordination was modified due to the presence of more layers of WO_x.

Summarizing: the reaction with the W chloroalkoxides provided the anatase nanocrystals with a layer of WO_x species. Such species had a tetrahedral environment and were bonded to the surface through Ti−O−W bonds. For $R > 0.16$, the surface was saturated, and the WO_x structures formed an amorphous layer around anatase. The cross-linking of the layer allowed the W cations to assume even octahedral environment, through the formation of small and poorly polymerized species.

After they were heated at 400 °C, the samples basically kept their structure (XRD). Above all, for $R_{0.64}$ the amorphous WO_x component persisted. Raman spectra show that the WO_x layer onto the anatase nanocrystals changed its structure, giving rise to a W═O Raman band at 977 cm^{-1} for $R_{0.16}$ and at 974 cm^{-1} for $R_{0.64}$. For high surface coverage, like that in the present work, these bands indicate a mixed environment of tetrahedral and octahedral sites.[34] In particular, the downshift of the W═O stretching with respect to the as-prepared samples indicated increased concentration of octahedral sites and, hence, more dense and cross-linked W oxide structures. This is in agreement with the appearance of the new "lattice" bands at very low frequencies and the intense bending band at ∼250 cm^{-1}. We finally note the rising background toward high frequencies, due to the organic residuals still present in the samples. In fact, they appeared bright brownish after the heat treatment, and FTIR spectra (discussed below) suggested the application of higher-temperature treatments. Moreover, the Raman spectra presented broad bands at ∼1400 and 1600 cm^{-1}, which are typical of graphite species, compatible with ongoing organics decomposition during the heat treatment.[45−47] Summarizing: the heat treatment at 400 °C, also due to the attenuation of the oleic acid capping, favored the cross-linking and densification of the WO_x phases for $R_{0.16}$ and $R_{0.64}$. The peculiar structure of the latter was confirmed by the complete absence of crystallization phenomena, very different from pure WO_3 nanocrystals prepared by the same precursor.[31]

After the sample was heated at 500 °C, the WO_x wrapping for $R_{0.64}$ was finally crystallized, as seen by XRD (Figure 1C), while for $R_{0.16}$ the surface layer of W oxide did not undergo obvious changes, demonstrating remarkable stability up to high temperatures. The presence of the surface layer had further consequence in the limitation of the grain growth, since the samples showed less enhanced peak narrowing with respect to pure TiO_2. The high-temperature treatment affected even the TiO_2 structure, as seen by the shift to lower angles of the XRD anatase peaks (Figure 1C). The Raman spectra confirmed the XRD interpretation. The structural modification induced by W was reflected in the shape of the anatase Raman bands, through their broadening and distortion, mainly for $R_{0.64}$, but it must be remarked that in all cases the Raman spectrum showed changes with respect to pure TiO_2. The position of the W═O Raman band was 974 cm^{-1} for both samples, indicating further redistribution of the W sites, in agreement with the XRD

DOI: 10.1021/acsami.5b00632
ACS Appl. Mater. Interfaces 2015, 7, 6898−6908

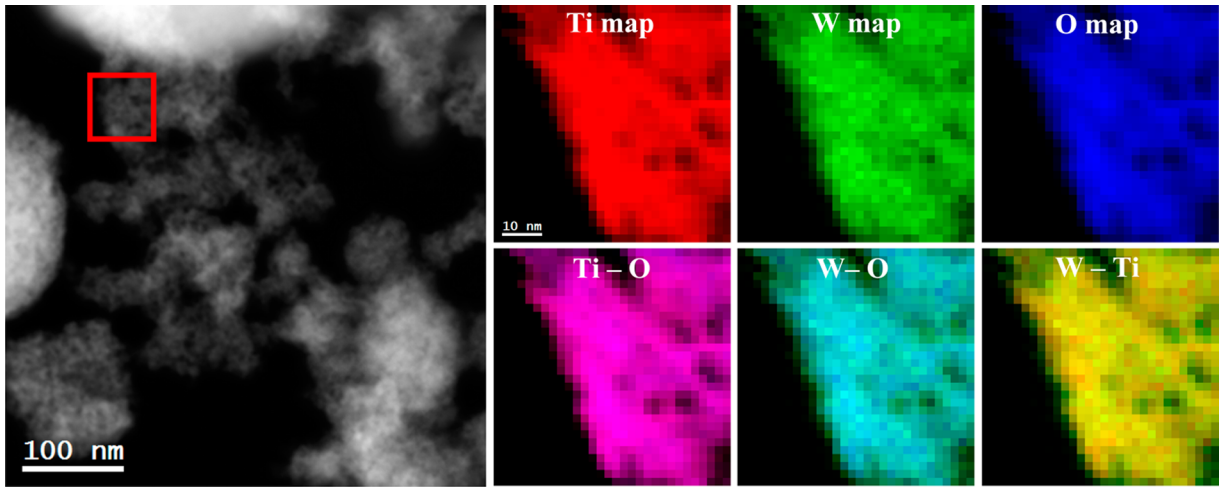

Figure 4. A general STEM-HAADF micrograph of the 500 °C $R_{0.64}$ and EELS maps of the red squared region: elemental Ti (red), W (green), and O (blue) maps and, in the bottom part, from left to right, composites of Ti−O, W−O, and W−Ti.

results. The main doubt concerned the fate of the amorphous WO_x layer for $R_{0.64}$ and its interaction with the anatase host material.

For further investigating this point, which was needed since the organics elimination and subsequent device processing required such 500 °C treatment, EELS investigation was performed on the corresponding sample. In Figure 4, a general STEM-HAADF micrograph and elemental EELS maps of the red squared region are presented. As seen in the color maps, the Ti, W, and O are distributed almost homogeneously throughout the nanoparticles. This result showed that after the heat-treatment at 500 °C the crystallized WO_3 material remained distributed over the TiO_2 phase, possibly resembling the previous wrapping structure. Nevertheless, it was difficult to directly visualize the WO_3 structures, as discussed for Figure 3. Because of the found differences in the TiO_2 lattice parameters, in agreement with the shift of the XRD peaks, it was concluded that part of tungsten diffused into the TiO_2 phase, as reinforced by the electrical data shown below. The WO_3 nanocrystals, as indicated by the related peaks in the XRD pattern in Figure 1C, may just be too small to be detected in the mass of the anatase host, which agglomerated after the removal of the oleic acid capping. The results shown introduce a remarkable difference with respect to previous works. In fact, the use of anatase nanocrystals, with a size that initially ranges ∼3 nm in the as-prepared samples, allowed complete wrapping by the gel-like WO_x component for $R_{0.64}$. This effect could obviously not be obtained with larger-sized TiO_2 materials. Summarizing: the heat treatment at 500 °C did not change the structure of the $R_{0.16}$ samples, still constituted by anatase nanocrystals that were surface-modified with WO_x, which did not undergo any phase segregation. The $R_{0.64}$ material was composed by a dispersion of tiny WO_3 nanocrystals around the surface-modified TiO_2 host. The TiO_2 itself was structurally modified by W doping. As a whole, changing the W concentration and using proper heat-treatment procedure, allowed exploration of a range of material architectures from naked anatase to surface coverage to heterojunctions.

2. Thermal Behavior of the Materials. Device processing requires heat treatment for thermal stabilization, since chemo-resistive gas sensors may require high-temperature operation, and hence prestabilization at a temperature higher than the maximum predicted operation conditions. Moreover, elimination of any organic residual is required for having a stable electric signal and improving the conductance. Optimization of the heat-treatment procedure may be performed by thermal analysis and checked by FTIR and Raman spectroscopy. While this topic is closely related to the device processing step and may be considered as a technological step, it also provided useful hints about the sample structure, so it will now be discussed in more detail. Figure 5 shows the results of the

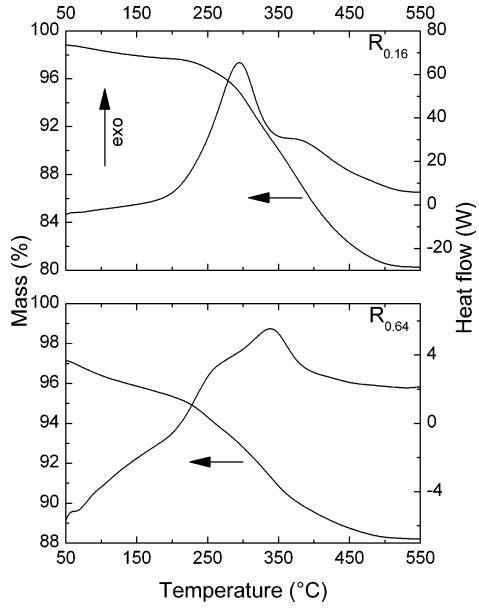

Figure 5. DSC-TG curves measured on the indicated samples. The mass variation is expressed as percentage of the initial value.

thermal analyses performed on the samples with different R_w values. For both samples, the mass loss reached a plateau at ∼500 °C, which suggested the correct temperature for heat treatment. As seen in the Raman section, this temperature ensured the absence of even graphitic carbon from organic pyrolysis. The thermogravimetric (TG) curve for $R_{0.64}$ had a more complex structure than that of $R_{0.16}$, reflecting the shape of the differential scanning calorimetry (DSC) analysis, composed of broad, overlapped peaks.

DOI: 10.1021/acsami.5b00632
ACS Appl. Mater. Interfaces 2015, 7, 6898−6908

Instead, the DSC value of the $R_{0.16}$ sample more closely resembled that of pure TiO_2.[28] These results were in agreement with a sample structure that, for $R_{0.16}$, was still basically constituted by anatase nanocrystals, while that for $R_{0.64}$ was remarkably affected by the structural evolution of the WO_x wrapping. In previous work on pure WO_3,[31] it was evidenced that the oleic acid capping was labile and easily eliminated even during the postsynthesis purification step. In the $R_{0.64}$ sample, hence, lower concentration of oleic acid would be initially present, since oleic acid will weakly coordinate to the WO_x wrapping layer. This explained that the overall mass loss for $R_{0.16}$ was larger than for $R_{0.64}$, due to the elimination of a larger concentration of the bulky oleic acid molecules. The IR spectra, shown in Figure 6, nicely confirmed the interpretation of the

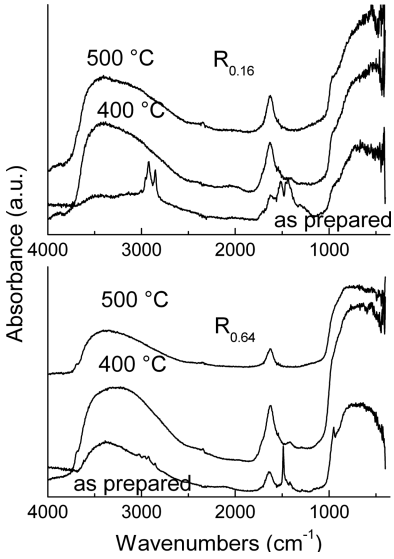

Figure 6. FTIR spectra measured on the $R_{0.16}$ and $R_{0.64}$ samples heat-treated at the indicated temperatures.

thermal data. From the device point of view, the organics elimination occurs after heating at 500 °C. But, above all, the alkyl bands in the as-prepared $R_{0.64}$ sample at ~3200 cm^{-1} (due to oleic acid) were almost absent, contrarily to the bands observed with $R_{0.16}$. Moreover, the OH signal in the as-prepared $R_{0.16}$ sample was much weaker than in the analogous $R_{0.64}$ spectrum: the more complex condensation and dehydration phenomena in $R_{0.64}$ were in agreement with the presence of various peaks and shoulders in the thermal data. The region around 1500 cm^{-1} contains characteristic features of the oleic acid molecule. In particular, the absence of the intense carbonyl band at 1709 cm^{-1} indicates the absence of dimeric oleic acid molecules (weak shoulders were observed in the 400 °C spectra, probably indicating residuals of free oleic acid not bonded to the surface) and complex formation through bridging/chelating modes.[48−50]

The separation, Δ, between the antisymmetric and symmetric stretching modes of the carboxylate ion in the 1500 cm^{-1} is useful for determining the type of coordination bonding.[51] In our case for both samples the Δ value was about 70 cm^{-1}, indicating a mixture of both configurations, in agreement with the presence of W species with different local symmetry onto the surface.

2. Gas-Sensing Properties of the Materials. The material architectures enabled by the synthesis process spanned a broad range of configurations, given the same TiO_2 guest phase, and the related sensing properties were investigated. Ethanol was chosen as a sample of reducing gas, capable of increasing the electrical conductance of the materials upon the sensing process. In Figure 7 the dynamic response curves of the

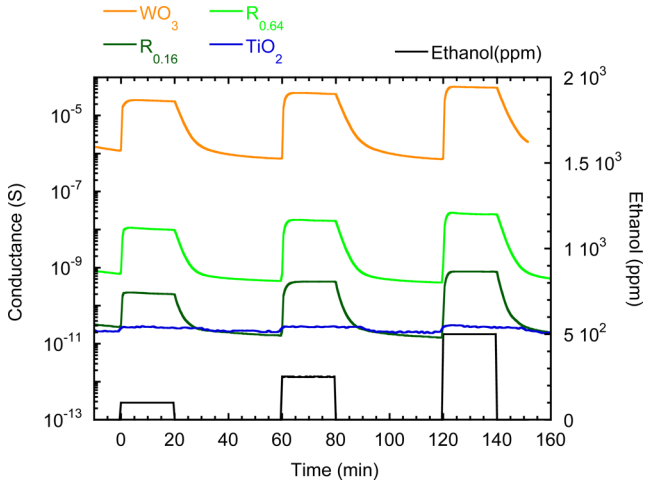

Figure 7. Dynamic response of the indicated sensors toward square concentration pulses of ethanol at a working temperature of 200 °C and 40% RH at 20 °C.

$R_{0.16}$ and $R_{0.64}$ materials heat-treated at 500 °C are reported, together with the analogous curves for pure TiO_2 and WO_3. First of all, we observe that pure TiO_2 and the $R_{0.16}$ sample had very similar base electrical conductance, at about 1×10^{-11} S. Instead, the $R_{0.64}$ sample had much higher conductance, by ~2 orders of magnitude.

This result is in agreement with the previously developed structural interpretation of the samples. In particular, the incorporation equations in Kröger−Vink notation are the following, for substitutional and interstitial WO_3 incorporation, respectively.

$$2WO_3 \rightarrow 2W_{Ti}^{\bullet\bullet} + 6O_O + V_{Ti}^{''''}$$

$$2WO_3 \rightarrow 2W_i^{6\bullet} + 6O_O + 3V_{Ti}^{''''}$$

where W_{Ti} and W_i indicate substitutional and interstitial W(VI) ions, V_{Ti} is a Ti vacancy, and O_O is an oxygen ion in regular lattice site. It can be seen that the formation of interstitial species requires the formation of a larger concentration of highly charged and energetically unfavorable Ti vacancies. Substitutional W(VI), whose presence in the $R_{0.64}$ sample was suggested by the modification of the structural parameters of TiO_2 and by the peak shift in the XRD patterns, would instead result in conductance increase by ionization of the loosely bound extra electrons in the anatase lattice. It is also striking that, by addition of only the WO_x surface layer for $R_{0.16}$, the electrical signal underwent a dramatic change upon ethanol introduction in the cell, differently from pure TiO_2 that displayed very weak variations. A similar effect occurred for $R_{0.64}$, having a different composition and structure from $R_{0.16}$.

The different responses were calculated and are displayed in Figure 8 for various operating temperatures. Note that, first of all, pure TiO_2 response slowly increased with increasing operating temperature. This trend was opposite to that of the TiO_2−WO_3 materials and evidenced catalytic effect of the WO_x surface modification, featuring low-temperature activation of

DOI: 10.1021/acsami.5b00632
ACS Appl. Mater. Interfaces 2015, 7, 6898−6908

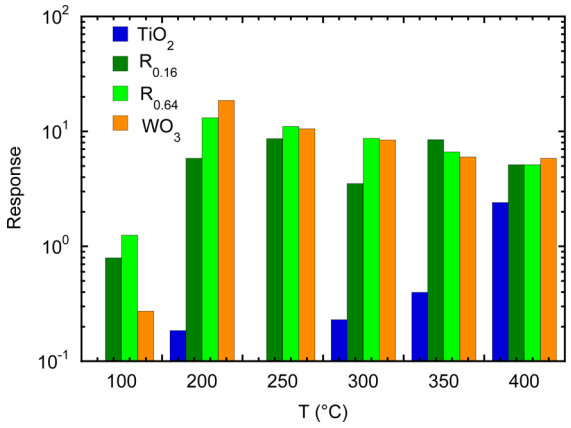

Figure 8. Response to 100 ppm of ethanol as a function of the operating temperature for the indicated sensors.

the sensing reactions. Hence, 200 °C resulted as the best operating temperature, where the W-modified materials provided the highest responses and simultaneous lowering of power consumption, in contrast to pure TiO_2, which was almost inactive at this temperature.

The response improvement of 2 orders of magnitude with respect to pure TiO_2 was the required proof of concept about the effectiveness of the W-surface modification. This situation was also confirmed for different ethanol concentrations at the best operating temperature of 200 °C, as shown in the calibration curves in Figure 9. The curves follow the typical

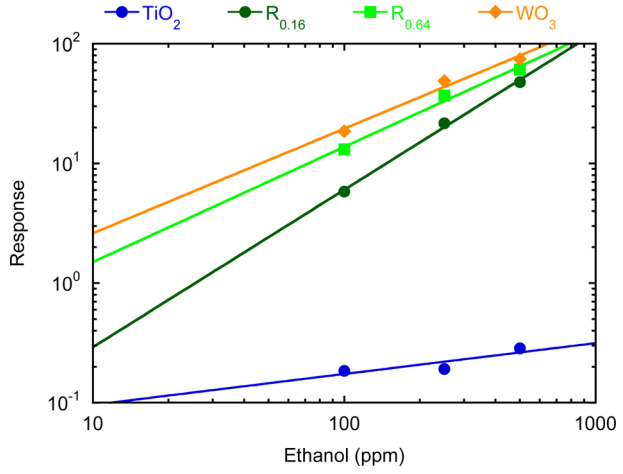

Figure 9. Calibration curve for ethanol of the indicated sensors at a working temperature of 200 °C.

power law[52] for chemoresistive gas sensors, giving a straight line on double logarithmic scale. What changes, apart for the already observed lower responses for pure TiO_2, is the slope of the curves. Both responses and slopes are grouped for pure WO_3 and the TiO_2–WO_x sensors; only, for $R_{0.16}$ the responses are slightly lower. Since the slope is related to the involved sensing mechanisms, the three materials have markedly different behavior from pure TiO_2: the proposed mechanism for ethanol sensing by SnO_2, based on a previous work by Kohl in 1991,[53,54] seems applicable, at least as an initial working hypothesis, and it is based on the formation of surface ethoxy groups and their transformation into acetaldehyde, which is then desorbed with hydrogen, or into rooted acetate groups. In our case, then, the surface W═O species would be favorable adsorption sites for ethanol, but we cannot exclude that the presence of W may induce different reaction pathways. In fact, the introduction of tungsten enhanced the sensing behavior of pure TiO_2 by providing its surface with species that, from the sensing point of view, were similar to pure WO_3. As we shall see below, the WO_3 nanocrystals in the $R_{0.64}$ may contribute to the increase of the base conductance and to the ethanol sensing, but the overall sensing properties for both W-modified sensors were dominated by the TiO_2 surface modification. Further hints about the role of the various components of the obtained materials could be obtained from the analysis of simple electrical properties. The related data are shown in Figures 10

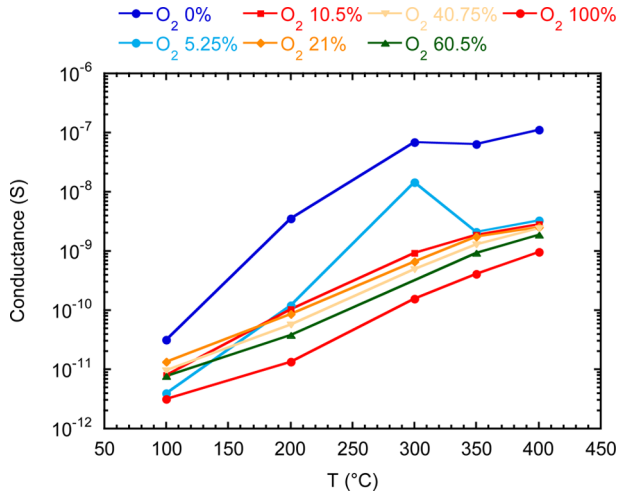

Figure 10. Electrical conductance data of the $R_{0.16}$ sample heat-treated at 500 °C as a function of the operating temperature and oxygen concentration.

and 11 for $R_{0.16}$ and $R_{0.64}$, respectively. The data have some common features, such as the increasing conductance with increasing temperature, in agreement with the n-type character of the prepared TiO_2-based materials, and a conductance decrease with increasing the oxygen concentration, for a given temperature, due to the oxygen adsorption/ionosorption and

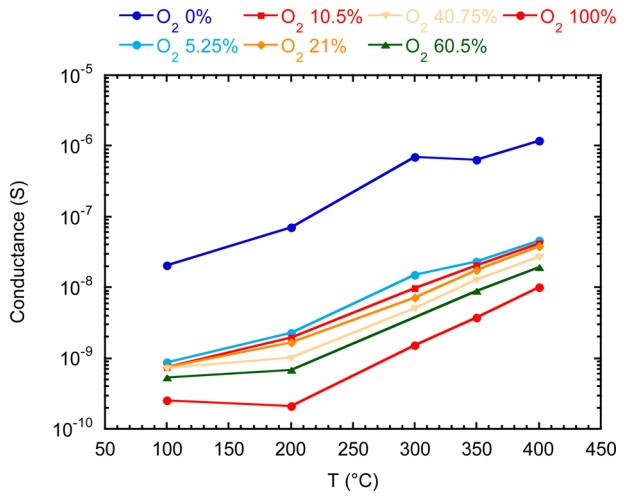

Figure 11. Electrical conductance data of the $R_{0.64}$ sample heat-treated at 500 °C as a function of the operating temperature and oxygen concentration.

DOI: 10.1021/acsami.5b00632
ACS Appl. Mater. Interfaces 2015, 7, 6898–6908

the consequent charge extraction from the materials conduction band. More interestingly, the oxygen introduction in the cell resulted in maximum conductance drops ranging ~3 orders of magnitude for both materials, at temperature starting from 200 °C, where additional adsorption phenomena (preadsorbed water, for instance) are less likely. This behavior is much different from that of pure TiO_2,[55] which is much less sensitive to oxygen concentrations and resembles much more that of pure WO_3.[31] On the other hand, the W incorporation equations show that the concentration of oxygen vacancies should be unaffected. So we conclude that the surface oxygen adsorption properties, which are fundamental in the gas-sensing behavior, are dominated by the presence of the W cations in the surface WO_x monolayers.

If we observe the conductance variations for both kinds of samples, for a given temperature and oxygen concentration, and keep into account the W doping for $R_{0.64}$, it seems that the WO_3 nanocrystals have a weak electrical effect in the $R_{0.64}$ sample, probably mainly acting as a baseline raising the conductance values with respect to $R_{0.16}$. The slightly higher response of the $R_{0.64}$ device may then be influenced by a similar additive term coming from the WO_3 nanocrystals.

CONCLUSIONS

The crystallization solvothermal processing of amorphous TiO_2 nanoparticles can be performed in the presence of a W chloromethoxide, whose concentration allows modifying the structure of the final product from surface modified to WO_x wrapped anatase TiO_2. The subsequent heat treatment results again in the surface-modified TiO_2 or in a dispersion of WO_3 nanocrystals into the TiO_2 guest phase, whose structure is further doped by W cations. From the analysis of the ethanol sensing and basic electrical data, it can be concluded that the surface modification of TiO_2 by monolayers of WO_x species activates the naked anatase species toward the oxidation of ethanol, while the WO_3 dispersed nanocrystals have an additive effect, improving the overall electrical conduction and providing additional gas response. We would finally like to comment about the choice between surface modification and heterojunctions. Surface modification in $R_{0.16}$ materials provided slightly lower sensing responses than those in $R_{0.64}$. On the other hand, the structure of $R_{0.16}$ was simpler than that of $R_{0.64}$, never featuring WO_3 phase segregation, even after heat treatment at 500 °C. This means that $R_{0.16}$ materials are intrinsically more stable than $R_{0.64}$, where the occurred phase segregation could induce further long-term modifications, such as growth of the WO_3 nanocrystals by coalescence, or by adsorption of W atoms from the TiO_2 nanocrystals. Moreover, the analysis of the data showed that for $R_{0.64}$ the response was slightly affected by the effect of a mechanical mixing of two phases, despite being on a very intimate size scale. Synergistic effects could only be attributed to anatase surface modification, present for both W concentrations, where the surface WO_x species create a more favorable oxidation/conductive channel with respect to pure TiO_2. Hence, the concept of heterojunction seems to be more applicable, in terms of defining a novel material architecture when real synergistic effects are present, than the simple physical proximity of two distinct phases.

ASSOCIATED CONTENT

Supporting Information

Further XRD patterns of as-prepared materials, complete Raman spectrum of the as-prepared $R_{0.16}$ sample, XPS spectra and data of the as-prepared materials, HRTEM of the 500 °C, $R_{0.64}$ sample, and NMR of as-prepared samples. This material is available free of charge via the Internet at http://pubs.acs.org.

AUTHOR INFORMATION

Corresponding Author

*E-mail: mauro.epifani@le.imm.cnr.it.

Notes

The authors declare no competing financial interest.

ACKNOWLEDGMENTS

Authors acknowledge CSIC/CNR Project No. 2010IT0001 (SYNCAMON) and the SOLAR Project No. DM19447. We thank G. B. Pace for the help with the sample preparation, and N. Poli for the help with the sensing measurements. J.A. and A.Z. acknowledge ICN2 Severo Ochoa Excellence Grant.

REFERENCES

(1) Engweiler, J.; Harf, J.; Baiker, A. WO_x/TiO_2 Catalysts Prepared by Grafting of Tungsten Alkoxides: Morphological Properties and Catalytic Behavior in the Selective Reduction of NO by NH_3. *J. Catal.* **1996**, *159*, 259−269.

(2) Forzatti, P.; Lietti, L. Recent Advances in De-NO(x)ing Catalysis for Stationary Applications. *Heterog. Chem. Rev.* **1996**, *3*, 33−51.

(3) Zhang, H.; Han, J.; Niu, X. W.; Han, X.; Wei, G. D.; Han, W. Study of Synthesis and Catalytic Property of WO_3/TiO_2 Catalysts for NO Reduction at High Temperatures. *Chem.—Eur. J.* **2011**, *350*, 35−39.

(4) Wachs, I. E.; Kim, T.; Ross, E. I. Catalysis Science of the Solid Acidity of Model Supported Tungsten Oxide Catalysts. *Catal. Today* **2006**, *116*, 162−168.

(5) Hino, M.; Arata, K. Superacids by Metal Oxides. 5. Synthesis of Highly Acidic Catalysts of Tungsten-Oxide Supported on Tin Oxide, Titanium-Oxide, and Iron-Oxide. *Bull. Chem. Soc. Jpn.* **1994**, *67*, 1472−1473.

(6) Lebarbier, V.; Clet, G.; Houalla, M. Relations between Structure, Acidity, and Activity of WO_x/TiO_2: Influence of the Initial State of the Support, Titanium Oxyhydroxide, or Titanium Oxide. *J. Phys. Chem. B* **2006**, *110*, 22608−22617.

(7) Patrono, P.; Laginestra, A.; Ramis, G.; Busca, G. Conversion of 1-Butene over WO_3-TiO_2 Catalysts. *Appl. Catal., A* **1994**, *107*, 249−266.

(8) Onfroy, T.; Lebarbier, V.; Clet, G.; Houalla, M. Quantitative Relationship between the Nature of Surface Species and the Catalytic Activity of Tungsten Oxides Supported on Crystallized Titania. *J. Mol. Catal. A: Chem.* **2010**, *318*, 1−7.

(9) Ulgen, A.; Hoelderich, W. F. Conversion of Glycerol to Acrolein in the Presence of WO_3/TiO_2 Catalysts. *J. Mol. Catal. A: Chem.* **2011**, *400*, 34−38.

(10) Akizuki, M.; Oshima, Y. Kinetics of Glycerol Dehydration with WO_3/TiO_2 in Supercritical Water. *Ind. Eng. Chem. Res.* **2012**, *51*, 12253−12257.

(11) Liebig, C.; Paul, S.; Katryniok, B.; Guillon, C.; Couturier, J. L.; Dubois, J. L.; Dumeignil, F.; Hoelderich, W. F. Glycerol Conversion to Acrylonitrile by Consecutive Dehydration over WO_3/TiO_2 and Ammoxidation over Sb-(Fe,V)-O. *Appl. Catal., B* **2013**, *132*, 170−182.

(12) Do, Y. R.; Lee, W.; Dwight, K.; Wold, A. The Effect of WO_3 on the Photocatalytic Activity of TiO_2. *J. Solid State Chem.* **1994**, *108*, 198−201.

(13) Keller, V.; Bernhardt, P.; Garin, F. Photocatalytic Oxidation of Butyl Acetate in Vapor Phase on TiO_2, Pt/TiO_2 and WO_3/TiO_2 Catalysts. *J. Catal.* **2003**, *215*, 129−138.

DOI: 10.1021/acsami.5b00632
ACS Appl. Mater. Interfaces 2015, 7, 6898−6908

(14) Puddu, V.; Mokaya, R.; Puma, G. L. Novel One Step Hydrothermal Synthesis of TiO_2/WO_3 Nanocomposites with Enhanced Photocatalytic Activity. *Chem. Commun.* **2007**, 4749−4751.
(15) Sajjad, A. K. L.; Shamaila, S.; Tian, B. Z.; Chen, F.; Zhang, J. L. One Step Activation of WO_x/TiO_2 Nanocomposites with Enhanced Photocatalytic Activity. *Appl. Catal., B* **2009**, *91*, 397−405.
(16) Yang, L. Y.; Si, Z. C.; Weng, D.; Yao, Y. W. Synthesis, Characterization and Photocatalytic Activity of Porous WO_3/TiO_2 Hollow Microspheres. *Appl. Surf. Sci.* **2014**, *313*, 470−478.
(17) Tsukamoto, D.; Ikeda, M.; Shiraishi, Y.; Hara, T.; Ichikuni, N.; Tanaka, S.; Hirai, T. Selective Photocatalytic Oxidation of Alcohols to Aldehydes in Water by TiO_2 Partially Coated with WO_3. *Chem.—Eur. J.* **2011**, *17*, 9816−9824.
(18) Szilagyi, I. M.; Forizs, B.; Rosseler, O.; Szegedi, A.; Nemeth, P.; Kiraly, P.; Tarkanyi, G.; Vajna, B.; Varga-Josepovits, K.; Laszlo, K.; Toth, A. L.; Baranyai, P.; Leskela, M. WO_3 Photocatalysts: Influence of Structure and Composition. *J. Catal.* **2012**, *294*, 119−127.
(19) Ramos-Delgado, N. A.; Gracia-Pinilla, M. A.; Maya-Trevino, L.; Hinojosa-Reyes, L.; Guzman-Mar, J. L.; Hernandez-Ramirez, A. Solar Photocatalytic Activity of TiO_2 Modified with WO_3 on the Degradation of an Organophosphorus Pesticide. *J. Hazard. Mater.* **2013**, *263*, 36−44.
(20) Ramos-Delgado, N. A.; Hinojosa-Reyes, L.; Guzman-Mar, I. L.; Gracia-Pinilla, M. A.; Hernandez-Ramirez, A. Synthesis by Sol-Gel of WO_3/TiO_2 for Solar Photocatalytic Degradation of Malathion Pesticide. *Catal. Today* **2013**, *209*, 35−40.
(21) Luevano-Hipolito, E.; Martinez-de la Cruz, A.; Lopez-Cuellar, E.; Yu, Q. L.; Brouwers, H. J. H. Synthesis, Characterization and Photocatalytic Activity of WO_3/TiO_2 for NO Removal under UV and Visible Light Irradiation. *Mater. Chem. Phys.* **2014**, *148*, 208−213.
(22) Patrocinio, A. O. T.; Paula, L. F.; Paniago, R. M.; Freitag, J.; Bahnemann, D. W. Layer-by-Layer TiO_2/WO_3 Thin Films as Efficient Photocatalytic Self-Cleaning Surfaces. *ACS Appl. Mater. Interfaces* **2014**, *6*, 16859−16866.
(23) Zhu, Y.; Su, X. T.; Yang, C.; Gao, X. Q.; Xiao, F.; Wang, J. D. Synthesis of TiO_2-WO_3 Nanocomposites as Highly Sensitive Benzene Sensors and High Efficiency Adsorbents. *J. Mater. Chem.* **2012**, *22*, 13914−13917.
(24) Miller, D. R.; Akbar, S. A.; Morris, P. A. Nanoscale Metal Oxide-Based Heterojunctions for Gas Sensing: A Review. *Sens. Actuators, B* **2014**, *204*, 250−272.
(25) Yang, X. L.; Dai, W. L.; Guo, C. W.; Chen, H.; Cao, Y.; Li, H. X.; He, H. Y.; Fan, K. N. Synthesis of Novel Core-Shell Structured WO_3/TiO_2 Spheroids and Its Application in the Catalytic Oxidation of Cyclopentene to Glutaraldehyde by Aqueous H_2O_2. *J. Catal.* **2005**, *234*, 438−450.
(26) de Castro, I. A.; Avansi, W.; Ribeiro, C. WO_3/TiO_2 Heterostructures Tailored by the Oriented Attachment Mechanism: Insights from Their Photocatalytic Properties. *CrystEngComm* **2014**, *16*, 1514−1524.
(27) Riboni, F.; Bettini, L. G.; Bahnemann, D. W.; Selli, E. WO_3-TiO_2 Vs. TiO_2 Photocatalysts: Effect of the W Precursor and Amount on the Photocatalytic Activity of Mixed Oxides. *Catal. Today* **2013**, *209*, 28−34.
(28) Epifani, M.; Diaz, R.; Force, C.; Comini, E.; Andreu, T.; Zamani, R. R.; Arbiol, J.; Siciliano, P.; Faglia, G.; Morante, J. R. Colloidal Counterpart of the TiO_2-Supported V_2O_5 System: A Case Study of Oxide-on-Oxide Deposition by Wet Chemical Techniques. Synthesis, Vanadium Speciation, and Gas-Sensing Enhancement. *J. Phys. Chem. C* **2013**, *117*, 20697−20705.
(29) Epifani, M.; Andreu, T.; Arbiol, J.; Diaz, R.; Siciliano, P.; Morante, J. R. Chloro-Alkoxide Route to Transition Metal Oxides. Synthesis of WO_3 Thin Films and Powders from a Tungsten Chloro-Methoxide. *Chem. Mater.* **2009**, *21*, 5215−5221.
(30) Epifani, M.; Comini, E.; Faglia, G.; Arbiol, J.; Andreu, T.; Pace, G.; Siciliano, P.; Morante, J. R. Two Step, Hydrolytic-Solvothermal Synthesis of Redispersible Titania Nanocrystals and Their Gas-Sensing Properties. *J. Sol-Gel Sci. Technol.* **2011**, *60*, 254−259.
(31) Epifani, M.; Comini, E.; Díaz, R.; Andreu, T.; Genç, A.; Arbiol, J.; Siciliano, P.; Faglia, G.; Morante, J. R. Solvothermal, Chloroalkoxide-Based Synthesis of Monoclinic WO_3 Quantum Dots and Gas-Sensing Enhancement by Surface Oxygen Vacancies. *ACS Appl. Mater. Interfaces* **2014**, *6*, 16808−16816.
(32) Daniel, M. F.; Desbat, B.; Lassegues, J. C.; Gerand, B.; Figlarz, M. Infrared and Raman-Study of WO_3 Tungsten Trioxides and WO_3, xH_2O Tungsten Trioxide Hydrates. *J. Solid State Chem.* **1987**, *67*, 235−247.
(33) Salvati, L.; Makovsky, L. E.; Stencel, J. M.; Brown, F. R.; Hercules, D. M. Surface Spectroscopic Study of Tungsten-Alumina Catalysts Using X-Ray Photoelectron, Ion Scattering, and Raman Spectroscopies. *J. Phys. Chem.* **1981**, *85*, 3700−3707.
(34) Horsley, J. A.; Wachs, I. E.; Brown, J. M.; Via, G. H.; Hardcastle, F. D. Structure of Surface Tungsten Oxide Species in the Tungsten Trioxide/Alumina Supported Oxide System from X-Ray Absorption near-Edge Spectroscopy and Raman Spectroscopy. *J. Phys. Chem.* **1987**, *91*, 4014−4020.
(35) Deo, G.; Wachs, I. E. Predicting Molecular-Structures of Surface Metal-Oxide Species on Oxide Supports under Ambient Conditions. *J. Phys. Chem.* **1991**, *95*, 5889−5895.
(36) Vuurman, M. A.; Wachs, I. E.; Hirt, A. M. Structural Determination of Supported V_2O_5-WO_3/TiO_2 Catalysts by in Situ Raman-Spectroscopy and X-Ray Photoelectron-Spectroscopy. *J. Phys. Chem.* **1991**, *95*, 9928−9937.
(37) Ramis, G.; Busca, G.; Cristiani, C.; Lietti, L.; Forzatti, P.; Bregani, F. Characterization of Tungsta-Titania Catalysts. *Langmuir* **1992**, *8*, 1744−1749.
(38) Scholz, A.; Schnyder, B.; Wokaun, A. Influence of Calcination Treatment on the Structure of Grafted WO_x Species on Titania. *J. Mol. Catal. A: Chem.* **1999**, *138*, 249−261.
(39) Reiche, M. A.; Burgi, T.; Baiker, A.; Scholz, A.; Schnyder, B.; Wokaun, A. Vanadia and Tungsta Grafted on TiO_2: Influence of the Grafting Sequence on Structural and Chemical Properties. *Appl. Catal., A* **2000**, *198*, 155−169.
(40) Yu, X.-F.; Wu, N.-Z.; Huang, H.-Z.; Xie, Y.-C.; Tang, Y.-Q. A Study on the Monolayer Dispersion of Tungsten Oxide on Anatase. *J. Mater. Chem.* **2001**, *11*, 3337−3342.
(41) Barreca, D.; Carta, G.; Gasparotto, A.; Rossetto, G.; Tondello, E.; Zanella, P. A Study of Nanophase Tungsten Oxides Thin Films by XPS. *Surf. Sci. Spectra* **2001**, *8*, 258−267.
(42) Jeon, S.; Yong, K. Synthesis and Characterization of Tungsten Oxide Nanorods from Chemical Vapor Deposition-Grown Tungsten Film by Low-Temperature Thermal Annealing. *J. Mater. Res.* **2008**, *23*, 1320−1326.
(43) Grabowska, E.; Sobczak, J. W.; Gazda, M.; Zaleska, A. Surface Properties and Visible Light Activity of W-TiO_2 Photocatalysts Prepared by Surface Impregnation and Sol−Gel Method. *Appl. Catal., B* **2012**, *117*−*118*, 351−359.
(44) Silversmit, G.; Doncker, G. D.; Gryse, R. D. A Mineral TiO_2 (001) Anatase Crystal Examined by XPS. *Surf. Sci. Spectra* **2002**, *9*, 21−29.
(45) Marcus, B.; Fayette, L.; Mermoux, M.; Abello, L.; Lucazeau, G. Analysis of the Structure of Multicomponent Carbon-Films by Resonant Raman-Scattering. *J. Appl. Phys.* **1994**, *76*, 3463−3470.
(46) Stair, P. C.; Li, C. Ultraviolet Raman Spectroscopy of Catalysts and Other Solids. *J. Vac. Sci. Technol., A* **1997**, *15*, 1679−1684.
(47) Tuinstra, F.; Koenig, J. L. Raman Spectrum of Graphite. *J. Chem. Phys.* **1970**, *53*, 1126−1130.
(48) Lee, D. H.; Condrate, R. A. FTIR Spectral Characterization of Thin Film Coatings of Oleic Acid on Glasses: I. Coatings on Glasses from Ethyl Alcohol. *J. Mater. Sci.* **1999**, *34*, 139−146.
(49) Yu, W. W.; Wang, Y. A.; Peng, X. G. Formation and Stability of Size-, Shape-, and Structure-Controlled CdTe Nanocrystals: Ligand Effects on Monomers and Nanocrystals. *Chem. Mater.* **2003**, *15*, 4300−4308.
(50) Young, A. G.; Al-Salim, N.; Green, D. P.; McQuillan, A. J. Attenuated Total Reflection Infrared Studies of Oleate and

DOI: 10.1021/acsami.5b00632
ACS Appl. Mater. Interfaces 2015, 7, 6898−6908

Trioctylphosphine Oxide Ligand Adsorption and Exchange Reactions on CdS Quantum Dot Films. *Langmuir* **2008**, *24*, 3841−3849.
(51) Deacon, G. B.; Phillips, R. J. Relationships between the Carbon-Oxygen Stretching Frequencies of Carboxylato Complexes and the Type of Carboxylate Coordination. *Coord. Chem. Rev.* **1980**, *33*, 227−250.
(52) Yamazoe, N.; Shimanoe, K. Theory of Power Laws for Semiconductor Gas Sensors. *Sens. Actuators, B* **2008**, *128*, 566−573.
(53) Kohl, D. Surface Processes in the Detection of Reducing Gases with SnO_2-Based Devices. *Sens. Actuators, B* **1989**, *18*, 71−113.
(54) Gurlo, A.; Riedel, R. In Situ and Operando Spectroscopy for Assessing Mechanisms of Gas Sensing. *Angew. Chem., Int. Ed.* **2007**, *46*, 3826−3848.
(55) Epifani, M.; Andreu, T.; Zamani, R.; Arbiol, J.; Comini, E.; Siciliano, P.; Faglia, G.; Morante, J. R. Pt Doping Triggers Growth of TiO_2 Nanorods: Nanocomposite Synthesis and Gas-Sensing Properties. *CrystEngComm* **2012**, *14*, 3882−3887.

DOI: 10.1021/acsami.5b00632
ACS Appl. Mater. Interfaces 2015, 7, 6898−6908